Science for Energy and Environment

Article

Constructing String-Cage Structure of α-MnO_2@CoS_2 Photoelectrocatalyst for Efficient Detoxification Sulfonamides Wastewater

Hongchao Ma [1,†], Yan Chen [1,†], Huizhen Jin [1,2,†], Xinyue Wang [3,*], Guowen Wang [1], Yinghuan Fu [1], Pengyuan Wang [1], Vadivel Subramaniam [4], Krishnamoorthy Ramachandran [5], and Xinghui Liu [2,6,7,*]

[1] School of Light Industry & Chemical Engineering, Dalian Polytechnic University, No. 1 Qinggongyuan, Ganjingzi District, Dalian 116034, China
[2] Science and Technology on Aerospace Chemical Power Laboratory, Hubei Institute of Aerospace Chemotechnology, Xiangyang 441003, China
[3] School of Textile and Material Engineering, Dalian Polytechnic University, No. 1 Qinggongyuan, Ganjingzi District, Dalian 116034, China
[4] Department of Physics, Saveetha School of Engineering, Saveetha Institute of Medical and Technical Sciences (SIMATS), Thandalam, Chennai 602105, Tamil Nadu, India
[5] Department of Physics, Faculty of Engineering and Technology, SRM Institute of Science and Technology, Vadapalani Campus, Chennai 600026, Tamilnadu, India
[6] Division of Research and Development, Lovely Professional University, Phagwara 144401, Punjab, India
[7] Hubei Provincial Key Laboratory of Artificial Quantum Two-Dimensional Materials, Hubei University of Technology, Wuhan 430068, P.R. China.
* Correspondence: wangxyyyy@163.com (X.W.); liuxinghui119@gmail.com (X.L.)
† These authors contributed equally to this work.

Received: 23 March 2025; Revised: 23 April 2025; Accepted: 3 June 2025; Published: 27 June 2025

Abstract: Constructing high-efficiency heterostructured photocatalysts for antibiotic degradation is critical and challenging. Herein, a "pearl necklace" α-MnO_2@CoS_2 photoelectrode was prepared via a continuous hydrothermal process. The as-obtained photoelectrode comprised overlong α-MnO_2 nanowires (as leading wire) and CoS_2 nanocages (as decorations) derived from ZIF-67 precursor. The contrivable α-MnO_2@CoS_2 photoelectrode exhibited lower charge transfer resistance and higher carrier separation efficiency than single α-MnO_2. The α-MnO_2@CoS_2 provided a heterostructured interface with fast carrier transfer, where α-MnO_2 nanowire played the carrier transfer channel, and the CoS_2 "nanocages" can effectively increase the contact area between the catalyst and the pollutants. Meanwhile, the stable p-n junction with the internal electric field can be formed in the synthesized α-MnO_2@CoS_2 composite to avoid the destruction of heterogeneous junctions and thus maintain stability. As a result, the α-MnO_2@CoS_2-0.2 had the highest PEC efficiency with a degradation rate of 98.95% for sulfonamides (SMX) within 50 min among prepared catalysts. The charge density difference of α-MnO_2@CoS_2 was performed to investigate the strong interaction between α-MnO_2 and CoS_2. This study provides insights into the construction of nanomaterial structures and their applicability to photocatalytic degradation of target pollutants, which can be expanded for future cost-effective water purification applications.

Keywords: α-MnO_2; CoS_2; photoelectrocatalysis; sulfamethoxazole; p-n heterojunction

1. Introduction

Sulfamethoxazole (SMX) is extensively utilized in animal husbandry and medicine as a prototypical broad-spectrum antimicrobial agent. Due to its high stability and hydrophilicity, SMX produces an inevitable and significant presence of residue in the treated wastewater and rivers (detection levels of μg/L–mg/L in wastewater treatment plants) [1,2]. The presence of toxic antibiotics not only disrupts the microbial ecological balance but also poses a significant threat to human health, in this case, pushes the advancement of effective degradation technologies in aquatic environments, including adsorption [3], membrane separation [4], coagulation [5], biodegradation [6] and advanced oxidation processes [7–9]. Among them, photoelectrocatalysis (PEC) technology has been considered as the promising solution for wastewater treatment, which combines photocatalysis (PC) with electrocatalysis (EC). By applying a bias voltage to the semiconductor photoanode under illumination and an external electric field, the recombination of photo generated electron hole pairs is effectively suppressed, thereby improving the photocatalytic activity of semiconductor photocatalysts [10,11]. Common photocatalytic semiconductor materials, such as TiO_2 [12], CdS [13], ZnS [14], and g-C_3N_4 [15], are generally hindered by slow migration of photogenerated electron-hole pairs and rapid carrier recombination, leading to low solar energy utilization and significant limitations in catalytic efficiency [16]. Additionally, two-dimensional materials such as MoS_2 and tungsten disulfide, despite their excellent optoelectronic properties, suffering from high raw material costs and poor process reproducibility, which further impede their large-scale implementation. Chi et al. [17] constructed coral-like WO_3/$BiVO_4$ photoanodes for detoxification of antibiotic wastewater by morphology and small surface engineering, the coral-like WO_3/$BiVO_4$ photoanode with the orientation growth of (110) and (011) active facets of $BiVO_4$ exhibited the optimal PEC performance due to significantly enhanced separation and transfer of photogenerated charge carriers. Thamilselvan et al. [18] synthesized the nickel-cobalt bimetallic ZIF (BMZIF) dodecahedron material. In the presence of peroxomonosulfate, it was able to completely degrade SMX within 24 min, which was attributed to the unique internal structure and the synergistic effect between ZIF and Ni/Co bimetals, resulting in improved light absorption and charge conduction efficiency. Following the previous studies, it can be found that the widespread commercialization and adoption of antibiotic degradation by PEC can only be realized by selecting suitable semiconductor material and structure to avoid photo-charge recombination [19,20]

In the current research, the commonly used photoelectrode semiconductors include TiO_2 [21,22], Fe_2O_3 [23], MnO_2 [24], WO_3 [25], and Bi_2MoO_6 [26,27]. Among them, MnO_2 is an N-type semiconductor with low cost and excellent photoresponse in both the ultraviolet and visible regions. Meanwhile, the α-MnO_2 crystallites exhibit higher performance, with larger specific surface area, electron transport, and higher manganese valence compared to another arrangement of MnO_2 octahedrons [28]. Moreover, the one-dimensional tunnel structure of α-MnO_2 facilitates complete contact with electrolytes, thereby exposing more catalytic active sites. However, its narrow band gap of 1.6–2.7 eV leads to easy recombination of electrons and holes [29]. To improve catalytic efficiency, photoelectrodes have been modified by various methods, among which nano-structure construction, doping engineering, surface modification, and heterostructure construction are the most commonly used strategies to improve photoelectrodes [30–32]. Among these, the design of heterojunction is crucial to optimize the catalytic activity of the electrode, which can prolong the duration of charge separation caused by the photoinduction process. And in various heterojunction configurations, the Z-scheme has a high reduction and oxidation ability, which is conducive to generating holes and free radicals [33–35].

In this case, metal-organic frameworks (MOFs), with the advantages of high porosity, low density, and large specific surface area, have been bi-functional materials with both sacrificial templates and metal precursors, which play an essential role in the construction of hollow micro/nanostructured materials with internal voids and functional shells [36,37]. Therefore, using the MOF template to prepare hollow structure materials and manufacture heterojunction with Z-type electron transport path is beneficial to charge transport and degradation performance. To meet the practical application of α-MnO_2 in antibiotic wastewater, selecting suitable materials for modification is necessary. Metal sulfides have been promising materials for PEC applications due to superior light absorption capacity, optical properties, and the structural tunability of their P-type and N-type behaviors [38]. The semi-metallic pyrite type Cobalt sulfide (CoS_2), as an abundant resource, has a modifiable Co electronic structure and a high degree of synergy between Co and S species and has been used as a photocatalyst for the degradation of polluted water [39,40].

Herein, we designed and synthesized a novel α-MnO_2 nanowire (NWs) composite MOF-derived CoS_2 nanocages (NCs) structure, in which NCs were formed on NWs with ZIF-67 as the sacrificial template and metal precursor, significantly increasing the specific surface area and conductivity of the material. Meanwhile, the shell thickness of the nanocages gradually thickens with the increase of vulcanization concentration, and the outer shell of the nanocages promotes electrolyte diffusion. The constructed p-n heterojunction reduced the recombination rate of electron-hole pairs, and the unique interweaving α-MnO_2 nanowires and CoS_2 nano hollow cage structures improved the charge transfer ability, which improved the overall PEC degradation performance. Combined with a series of electrochemical characterization and energy band analysis, the optimized α-MnO_2@CoS_2-0.2 electrode had excellent electron transfer capability in theory, consistent with the results of SMX degradation tests. Furthermore, the interaction between α-MnO_2 and CoS_2 was also analyzed using density functional theory to determine the electron transfer pathway.

2. Results and Discussion

2.1. Structural Characteristics

The synthesis process of Ti/α-MnO_2@CoS_2 one-dimensional axial layer structure was shown in Scheme 1. Cobalt ions were adsorbed on the pre-prepared α-MnO_2 (negatively charged) surface to provide nucleation sites for forming ZIF-67 by electrostatic interaction [41]. Finally, after solvent heat treatment during vulcanization, MOF-derived layered α-MnO_2·@CoS_2 were formed. It is worth noting that when controlling the amount of thioacetamide (TAA) during vulcanization, the case thickness of CoS_2 NCs gradually increased.

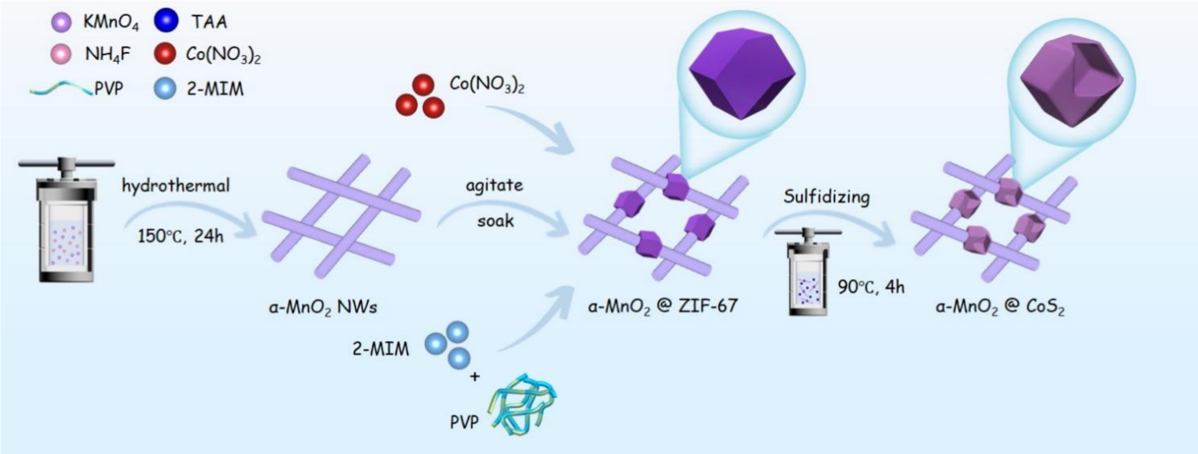

Scheme 1. The synthesis procedures of hollow core-shell heterostructure α-MnO_2@CoS_2 electrode material on Ti sheet.

The successful synthesis of heterojunction structures was confirmed by X-ray diffraction (XRD), and then the coating of α-MnO_2 nanowires with different concentrations of CoS_2 nanocages was investigated. The prominent diffraction peaks were 12.7°, 18.1°, 25.7°, 28.8°, 37.5°, 41.2°, 60.3°, 69.7° and 77.2° correspond to the (110), (200), (220), (310), (211), (420), (521), (541) and (402) crystal faces of α-MnO_2 (JCPDS no. 44-0141) (Figure S1). After the electrostatic adsorption of cobalt ions, the emergence of diffraction peaks of ZIF-67 crystal and the intensity of α-MnO_2 diffraction peak decreased, indicating that a large number of ZIF-67 nanoparticles successfully encapsulate α-MnO_2, which proved the successful synthesis of the intermediate Ti/α-MnO_2@ZIF-67. After solvent heat treatment during vulcanization, it can be found that the diffraction peak of ZIF-67 disappeared, and with the emergence of diffraction peaks of 27.6°, 32.3°, 60.2° corresponding to (111), (200), (230) crystal faces of CoS_2 (JCPDS no. 41-1471), ascribed to the synthesis of core-shell heterostructure α-MnO_2@CoS_2. Then, the core-shell structure surface was changed when different amounts of TAA were added to vulcanization (Table S1; named α-MnO_2@CoS_2-0.1 for using 0.1 mmol TAA precursors, named α-MnO_2@CoS_2-0.2 for using 0.2 mmol TAA precursors, named α-MnO_2@CoS_2-0.3 for using 0.3 mmol TAA precursors, named α-MnO_2@CoS_2-0.4 for using 0.4 mmol TAA precursors) (Figure S2). It can be seen that the position of the peak would not change significantly, indicating that its structural composition did not change. With the sulfide increase, the diffraction peak of α-MnO_2 gradually decreased, indicating that the rise of TAA caused the case thickness of CoS_2 nanocages to increase progressively, covering the surface of α-MnO_2 lines.

Then, the heterostructure surface was observed by scanning electron microscopy (SEM) (Figure 1), and the prepared α-MnO_2 had a nanowire structure with a diameter of about 20–50 nm. The ZIF-67 nanopolyhedra with diameters of 200–300 nm was uniformly encapsulated on the surface of the α-MnO_2 NWs to form a layered core-shell nanostructure (Figure 1b). The ZIF-67 assembled in the outer layer of the α-MnO_2 became a hollow nanocage and inherited the shape of the original ZIF-67 structure. Subsequently, it was found that the amount of TAA had an essential effect on the microstructure and properties of the composites. A similar hollow nanocage structure was formed when the amount of TAA was reduced to 7.531 mg. In contrast, the surface of the hollow nanocage was relatively thin (Figure 1c). However, with the increase in TTA dosage, the thickness of the nanocage case gradually increased, and some nanoparticles were deposited on the surface of the nanocages. The nanocages were gradually agglomerated (Figure 1d–f). The corresponding EDS-mapping of α-MnO_2@CoS_2-0.2 (Figure 1g) showed that Mn was distributed only along the nanowires. In contrast, S, Co, and O were distributed along the nanocage shell, further confirming the core-shell structure of the catalyst.

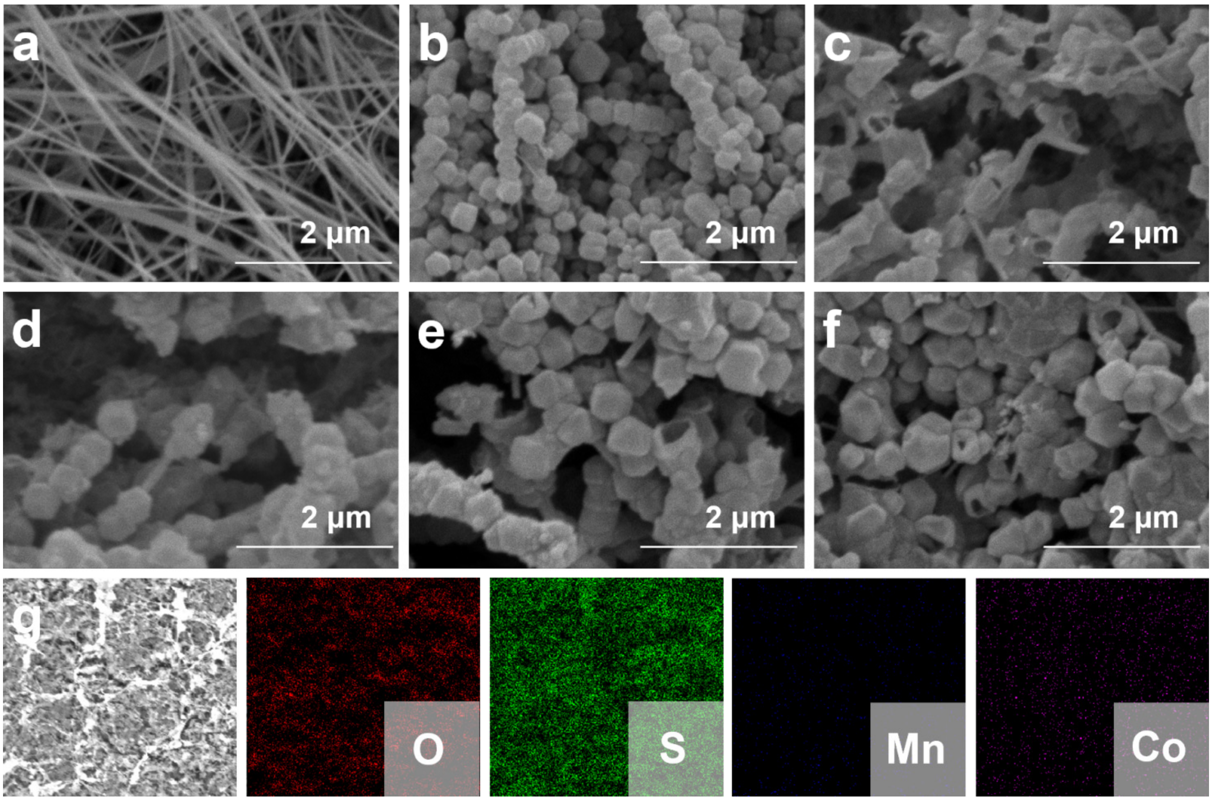

Figure 1. SEM images of as-prepared electrodes. (**a**) α-MnO_2; (**b**) α-MnO_2@ZIF-67; (**c**–**f**) α-MnO_2@CoS_2-x (x = 0.1, 0.2, 0.3, 0.4); (**g**) elemental EDS mapping (Mn, O, S and Co) analysis of α-MnO_2@CoS_2-0.2.

The spatial distribution of CoS_2 and α-MnO_2 in the α-MnO_2@CoS_2 sample was investigated by transmission electron microscopy (TEM) (Figure 2). It could be seen more clearly that α-MnO_2 plays the role of nuclear support in the composite structure. The simultaneous appearance of branches can provide more paths for electrons to accelerate and move in parallel (Figure 2a). Moreover, the CoS_2 nanocages were exclusively enveloped around the α-MnO_2 surface, creating a stable heterojunction structure. In high-resolution transmission electron microscopy (HRTEM) images, the fringe spacings of 0.40 nm and 0.16 nm correspond to the α-MnO_2 (310) and CoS_2 (200) crystal planes, respectively (Figure 2b), further confirming the formation of the core-shell structure. In addition, EDS spectroscopy was also performed on both compositions, which showed that CoS_2 was distributed in the heterojunction structure as a porous structure, while the columnar α-MnO_2 acted as an electron transport channel, in agreement with previous SEM results (Figure 2c–f).

X-ray photoelectron spectroscopy (XPS) was used to gain insight into the chemical state of the elements in α-MnO_2@CoS_2-0.2. The total XPS spectrum of α-MnO_2@CoS_2-0.2 (Figure S3) showed the presence of Mn, O, Co, and S elements, which agreed with the EDS results. The three pairs of splitting peaks in the Mn 2p XPS spectra of α-MnO_2@CoS_2-0.2 and MnO_2 (Figure 3a) can be attributed to the Mn $2p_{3/2}$ and Mn $2p_{1/2}$ signals of Mn (IV), Mn (III), and Mn (II), respectively. Specifically, the peaks at 643.60~643.70 eV and 654.70~654.80 eV belonged to Mn (IV) (Mn $2p_{3/2}$ and Mn $2p_{1/2}$), the peaks at 642.14~642.24 eV and 653.65~653.75 eV belonged to Mn (III) (Mn $2p_{3/2}$ and Mn $2p_{1/2}$) and the two peaks at 641.20~641.30 eV and 652.60~652.70 eV belonged to Mn (II) (Mn $2p_{3/2}$ and Mn $2p_{1/2}$), which confirmed that Mn (IV), Mn (III), and Mn (II) coexisted in α-MnO_2@CoS_2-0.2. The negative shift of the Mn 2p peak to α-MnO_2 in α-MnO_2@CoS_2 demonstrated the transfer of electrons from CoS_2 to α-MnO_2, confirming the photogenerated carrier transfer pathway of the Z-scheme heterojunction caused by the driving recombination force. Then, the three peaks at 529.45~530.78 eV (S1), 531.00~531.59 eV (S2), and 532.00~532.41 eV (S3) represented lattice oxygen, functional groups or defect sites, and surface adsorbed oxygen, respectively (Figure 3b). It was evident that the introduction of CoS_2 increase the area of S1 (α-MnO_2@CoS_2), indicating that the enhancement of the adsorption capacity of reactive oxygen species on the surface of the composite material is conducive to optimizing the performance of PEC. It was noteworthy that the binding energy of the Mn 2p and Co 2p spectra of α-MnO_2@CoS_2-0.2 moved due to the electronic interaction between α-MnO_2 NWs and CoS_2 NCs, which effectively regulates the electronic structure on the surface of α-MnO_2 and forms electron-deficient and electron-rich regions near CoS_2 and α-MnO_2, respectively, promoting the effective catalytic degradation of SMX [42]. Furthermore, the Co 2p spectrum (Figure 3c) provides insights into the Co 2p characteristics of CoS_2, exhibiting two pairs of splitting peaks along with two satellite peaks. The splitting peaks at 778.84~778.94 eV and 781.36~781.46 eV correspond to the Co $2p_{3/4}$, while those at 793.90~794.00 eV and 797.58~797.68 eV were associated with the Co $2p_{1/2}$, confirming the formation of CoS_2 nanoparticles on the α-MnO_2 surface. Compared with sole α-MnO_2, the binding energy of Co 2p spectra of the composite catalyst shifted positively, which may be due to the strong electron interaction between α-MnO_2 nanowires and CoS_2 nanosheets, resulting in a decrease in electron density on the surface of the CoS_2 nanocages and further confirming the formation of the Z-scheme heterojunction. Regarding the S 2p peaks, the values at 162.15~162.2 eV and 163.57~163.62 eV can be assigned to the S $2p_{3/2}$ and S $2p_{1/2}$ orbits of CoS_2, respectively (Figure 3d). In addition, the peaks at 168.56~168.61 eV and 169.66~169.71 eV were typical surface sulfur oxides (S-O), which may be caused by oxygen adsorbing from the active surface, benefiting for the degradation treatment of pollutants.

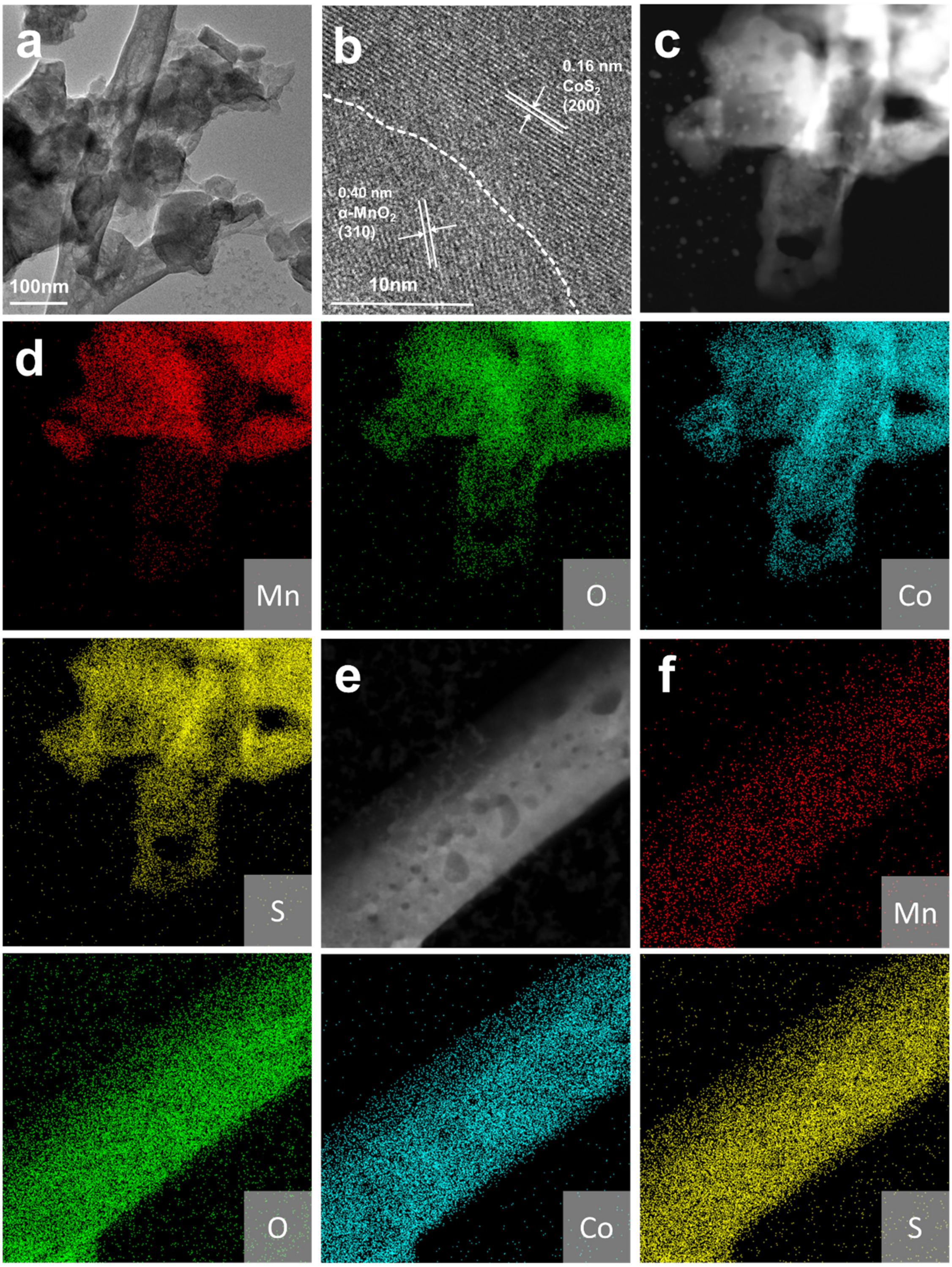

Figure 2. (**a**)TEM image of α-MnO_2@CoS_2; (**b**) High-resolution TEM image of α-MnO_2@CoS_2-0.2; (**c**–**f**) elemental EDS mapping analysis of α-MnO_2@CoS_2-0.2.

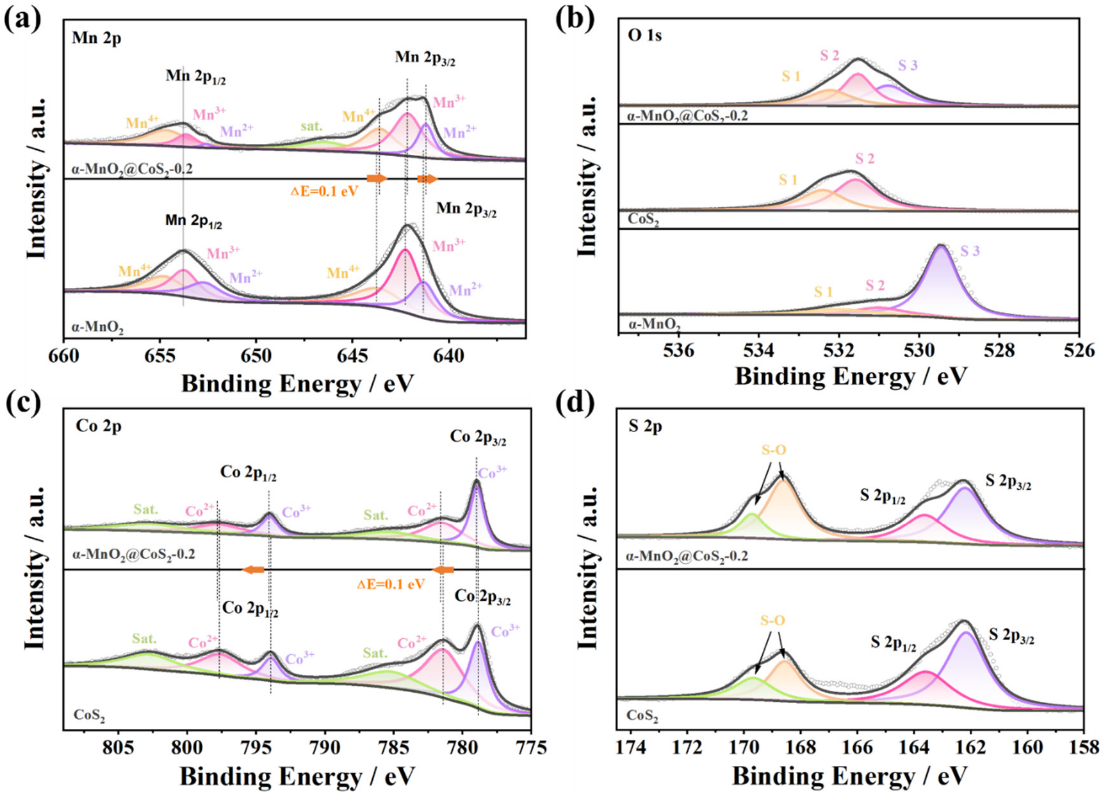

Figure 3. XPS spectra for α-MnO_2, CoS_2, and α-MnO_2@CoS_2-0.2: (**a**) high-resolution Mn 2p XPS spectra; (**b**) high-resolution O 1s XPS spectra; (**c**, **d**) high-resolution Co 2p and S 2p XPS spectra.

2.2. Electrochemical Performance Analysis

With the ideal structure, the electrochemical properties of α-MnO_2 and various α-MnO_2@CoS_2-(0.1, 0.2, 0.3, 0.4) electrodes were investigated in neutral media (Figure 4). Oxygen evolution potential (OEP) is a fundamental feature of anode applications, which was studied by linear sweep voltammetry (LSV). The results indicated that α-MnO_2@CoS_2-0.2 exhibited the highest OEP value (Figure 4a). This finding confirmed that the optimal loading of CoS_2 nanoparticles can prevent the interaction of active oxygen species adsorbed on the electrode surface, reduce the side reaction current, and enhance the PEC degradation efficiency of the entire electrode.

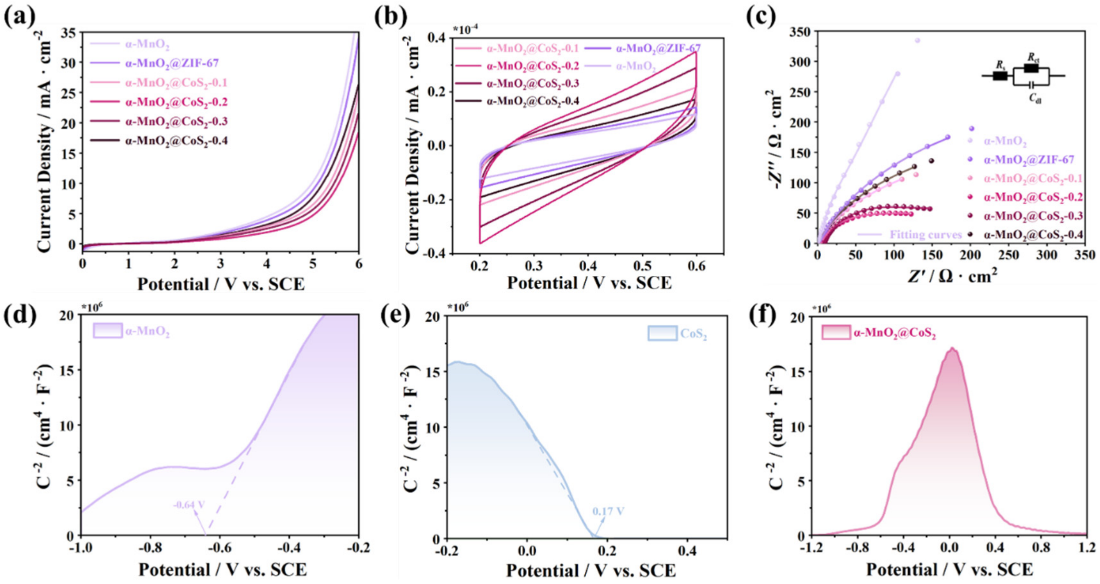

Figure 4. The electrochemical characterization of α-MnO_2 and various α-MnO_2@CoS_2-x electrodes: (**a**) Polarization curves; (**b**) Cyclic voltammograms; (**c**) EIS measurement results and the simulated circuit. Dots and lines represent the experimental and simulated data, respectively. Mott-Schottky plots of (**d**–**f**) α-MnO_2, CoS_2, andα-MnO_2@ CoS_2-0.2.

At the scan rate of 5 mV s^{-1}, the active area of the PEC electrode was evaluated by cyclic voltammetry (CV) testing (Figure 4b). The number of active sites in the electrode material is usually determined by observing the effective area of the voltammetry characteristic curve, where the active surface area of the anode oxide is proportional to the voltammetry charge [43]. Compared with the single-phase α-MnO_2 electrode, the enclosed area of the CV curve of α-MnO_2@CoS_2-0.2 electrode was larger, indicating stronger electrocatalytic ability and relatively good potential for catalyzing antibiotic oxidation. Electrochemical impedance spectroscopy (EIS) (Figure 4c) was used for surface charge transfer kinetics analysis from the Nyquist curve. If the Nyquist diagram exhibits a semicircular shape, it generally indicates that carrier transfer is occurring. A small radius of the semicircle suggests a low resistance to electron transfer, often attributed to oxygen vacancies [44]. Compared with other electrodes, α-MnO_2@CoS_2-0.2 had a small impedance arc diameter and a low charge transfer resistance (R_{ct}), corresponding to the faster interfacial electron transfer rate capability. At the same time, the transient photocurrent response can further prove that the charge transfer ability of α-MnO_2@CoS_2-0.2 at the catalyst/electrolyte interface was significantly improved (Figure S4). Under dark conditions, all five photoelectrodes exhibited essentially no current. However, the initial peak of the anode photocurrent was observed to form at the instant light was introduced, which was attributed to the accumulation of electrons (CB). Over time, the resulting photocurrent decreased exponentially until a stable current was reached due to the electron recombination process [45]. However, α-MnO_2@CoS_2-0.2 had the highest photocurrent density and the fastest photocurrent response with the best reproducibility. Overall, the photoelectric activity test showed that α-MnO_2@CoS_2 heterojunction not only improves the photo-responsiveness but also improved the surface reactivity of the photoelectrode, in which α-MnO_2@CoS_2-0.2 had the best performance.

The type and band potential (E_{fb}) of a semiconductor can be characterized by the Mott-Schottky (M-S) diagram (Figure 4d–f) [46]. The M-S test showed that the slope of the α-MnO_2 curve was positive, indicating that the electrode had N-type semiconductor characteristics. In contrast, the slope of the CoS_2 curve was negative, indicating that the electrode had the attributes of a P-type semiconductor. When constructing a p-n junction, the Mott-Schottky plot for α-MnO_2@CoS_2-0.2 presented an inverted "V" shape (Figure 4f). In general, the E_{VB} of P-type semiconductors was very close to E_{fb} (about 0.2 eV lower than E_{VB}), while the E_{CB} of N-type semiconductors was very close to E_{fb} (about 0.2 eV higher than E_{CB}) [47,48]. It could be confirmed that the E_{fb} of α-MnO_2 and CoS_2 were −0.64eV (−0.40V vs. NHE) and 0.17eV (0.41V vs. NHE), respectively. To more clearly elucidate the band characteristics of the catalyst, the band gaps were calculated by analyzing the different semiconductor electrodes' UV-Vis diffuse reflectance spectra (DRS) (Figure S5). It can be seen that the E_{CB} of α-MnO_2 and E_{VB} of CoS_2 were −0.60 V (vs. NHE) and 0.61 V (vs. NHE), respectively. According to $E_{VB} = E_{CB} + E_g$, the corresponding E_{VB} and E_{CB} values for α-MnO_2 and CoS_2 can be estimated as 1.43 V (vs. NHE) and −1.71 V (vs. NHE) and the proposed band structures of α-MnO_2@CoS_2 as shown in Figure S6.

2.3. Degradation Performance

The concentration change of SMX during degradation was monitored by high-performance liquid chromatography. For the specific detection method, refer to the Supplementary information. First, the performance of single electrode and composite electrode was tested through electrocatalytic (EC), photocatalytic (PC), and photocatalytic (PEC) degradation processes, respectively (Figure 5a). The results showed that the degradation effect of the composite electrode was better than that of single electrode among the three oxidation techniques, indicating that the formation of heterojunction structure was conducive to the formation and migration of active oxygen species. In addition, for the constant photoelectrode, the degradation rate of SMX during PEC was significantly increased, which was better than PC and EC, even the sum of them. This can be attributable to the synergistic effect of PEC, which was conducive to improving the photodynamic coupling efficiency based on lower exogenous energy [49]. Then, the PEC degradation of SMX by different α-MnO_2@CoS_2-x composite electrode structures was tested. It could be seen that α-MnO_2@CoS_2-0.2 had the highest PEC degradation efficiency (degradation rate within 50 min was 98.95%), consistent with the conclusion obtained in Structural characteristics (Figure 5b). The degradation effect of SMX was significantly improved with the increase of nanocage density on the surface of α-MnO_2 nanowire, which was due to the formation of composite structure, which increased the effective area of catalyst electrode. α-MnO_2@CoS_2 showed the best effect. However, when the CoS_2 precursor concentration continued to increase, its degradation rate decreased significantly, which may be due to excessive adsorption leading to blockage on the electrode surface. At the same time, the increase of the resistivity of the material with the thickness will hinder the transmission of the carrier, reduce the effective removal efficiency of the external circuit to the photogenerated electrons, resulting in poor degradation effect. Combined with structural analysis, this may be because CoS_2 hollow nanocages with high porosity can fully contact with the target pollutant SMX, which was conducive to the rapid movement of carriers and the improvement of PEC activity.

To determine the main active substances in the degradation process of PEC, free radical capture experiments were conducted (Figure 5c). Specifically, isopropanol (IPA), ethylenediamine tetraacetic acid disodium salt (EDTA-2Na), tryptophan (trp), and L-ascorbic acid (LA) are used as inhibitors of hydroxyl radicals (•OH), holes (h^+), singlet oxygen ($^1O_2$), and superoxide radicals ($•O_2^-$), respectively. •OH possess extremely high reactivity and can react with hydrogen atoms in IPA, thereby being scavenged by IPA. This reaction deactivates the •OH, preventing them from participating in further oxidation reactions and thus inhibiting their oxidative effect on target substances. During photocatalysis, h^+ typically react with metal ions or water molecules on the catalyst surface to generate highly oxidative species. EDTA-2Na can bind to these metal ions or active sites, preventing the interaction between h^+ and them, thereby suppressing the oxidative ability of h^+. The indole ring of trp can undergo energy transfer or chemical reactions with $^1O_2$, reducing the energy of $^1O_2$ and converting it into ordinary triplet oxygen ($^3O_2$), thereby losing its high reactivity. $•O_2^-$ can undergo redox reactions with LA, where the LA is oxidized and the $•O_2^-$ are reduced to water or other more stable substances, thereby suppressing the oxidative capacity of the superoxide anion radicals. After adding EDTA-2Na and IPA, the efficiency of PEC did not decrease significantly, indicating that h^+ and •OH had little influence on the reaction. It was worth noting that after the addition of trp and LA, the degradation efficiency of α-MnO_2@CoS_2-0.2 was significantly inhibited and significantly decreased to 39.7% and 47.9%, indicating that $^1O_2$ and $•O_2^-$ were the main active substances involved in SMX degradation. In addition, it could be carried out a cyclic experiment on the composite electrode to test the stability of the electrode, as shown in Figure 5d. After five degradation cycles, the degradation rate of SMX by α-MnO_2@CoS_2-0.2 remained at about 71.87%, indicating the reusability of electrode materials. In addition, XRD and SEM analysis showed that the crystal structure and composition of α-MnO_2@CoS_2-0.2 remained unchanged during the durability test (Figure S7). The positions of the peaks before and after the reaction did not shift or disappear significantly, indicating structural stability. Compared with recently reported α-MnO_2-based nanomaterials (Table S2), the α-MnO_2@CoS_2-0.2 exhibits outstanding PEC degradation performance.

Additionally, we performed the charge density difference of α-MnO_2@CoS_2 based on the density functional theory to investigate the interaction between α-MnO_2 and CoS_2 (Figure 5e) [50–52]. In Figure 5f, yellow represented receiving electrons and cyan represented providing electrons. The direction of charge transfer between the two can be seen through the obtained plane average differential charge density. On the side of the interface near CoS_2, there was a prominent peak of charge accumulation, and on the side near α-MnO_2, the charge loss was also pronounced near ~5 angstroms, which once again proved the trend of CoS_2 transfer to α-MnO_2. Thus, from the calculation results, we can conclude that α-MnO_2 taken electrons from CoS_2 were consistent with the charge carrier's migration of the Z-scheme mechanism.

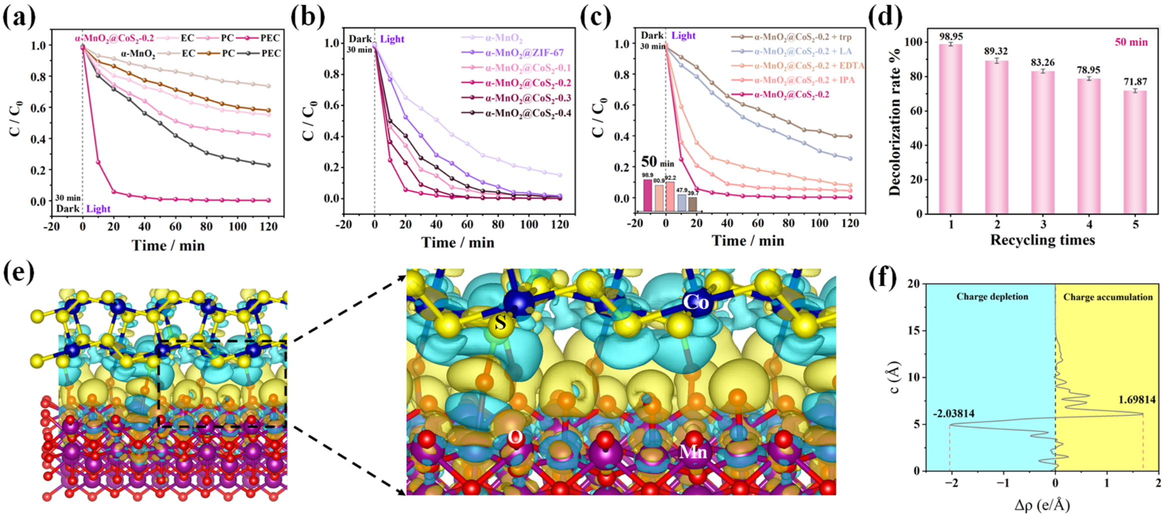

Figure 5. (**a**) SMX removal efficiency comparation of α-MnO_2, α-MnO_2@CoS_2-0.2 at different reaction conditions (PC, EC and PEC) after 120 min; (**b**) PEC degradation curves of SMX with different α-MnO_2@CoS_2-x composite electrodes; (**c**) Evaluation of active species in PEC process toward degradation of antibiotic SMX using α-MnO_2@CoS_2-0.2; (**d**) Five recycling experiments of α-MnO_2@CoS_2-0.2; (**e**) Charge density difference of α-MnO_2@CoS_2; (**f**) Planar-averaged differential charge density (Δρ) of α-MnO_2@CoS_2.

2.4. Mechanism of PEC Degradation

Anchored on the estimation of the band positions of α-MnO_2 and CoS_2, the possible type Z- scheme of the enhanced photocatalytic performance of α-MnO_2@CoS_2 can be obtained as shown in Scheme 2. When the α-MnO_2@CoS_2-0.2 composite is exposed to visible light, both α-MnO_2 and CoS_2 can be excited, producing electron and hole (e^-/h^+) pairs. Assuming the type II configuration holds, the electrons induced by CoS_2 in CB tend to transfer to CB of α-MnO_2 due to potential difference, while the holes induced in VB go in the opposite direction. However, the oxidation potential of VB in CoS_2 (0.61vs. NHE) would be not enough to oxidize O_{2g} and $\bullet O_2^-$ to generate H_2O_2 and $^1O_2$ (E (O_{2g} /H_2O_2) = 0.68V (vs. NHE), E ($\bullet O_2^-$/$^1O_2$) = 0.95 (vs. NHE). If, in this case, the α-MnO_2@CoS_2 heterostructure could not produce the $^1O_2$ obtained by the capture test, the hypothesis would not be valid. Due to the stable p-n junction formed in the α-MnO_2@CoS_2 composite, which followed Z-scheme, e^- in CB of α-MnO_2 was transferred to CB of CoS_2 with the help of the internal electric field, thereby inhibiting the recombination of interfacial charge carriers. From the energy level diagram, we also found that O_2 could easily capture electrons on CB of CoS_2 and the movement of an internal electric field to generate free radicals ($\bullet O_2^-$), which was consistent with the detection result of the free radical capture experiment. Then, the generated $\bullet O_2^-$ would further react to generate $^1O_2$ with the accumulation of h^+ in the VB of α-MnO_2. Moreover, the remaining e^- in CoS_2 CB was captured by dissolved oxygen or catalyst surface oxygen and converted into $\bullet O_2^-$ which can also degrade SMX.

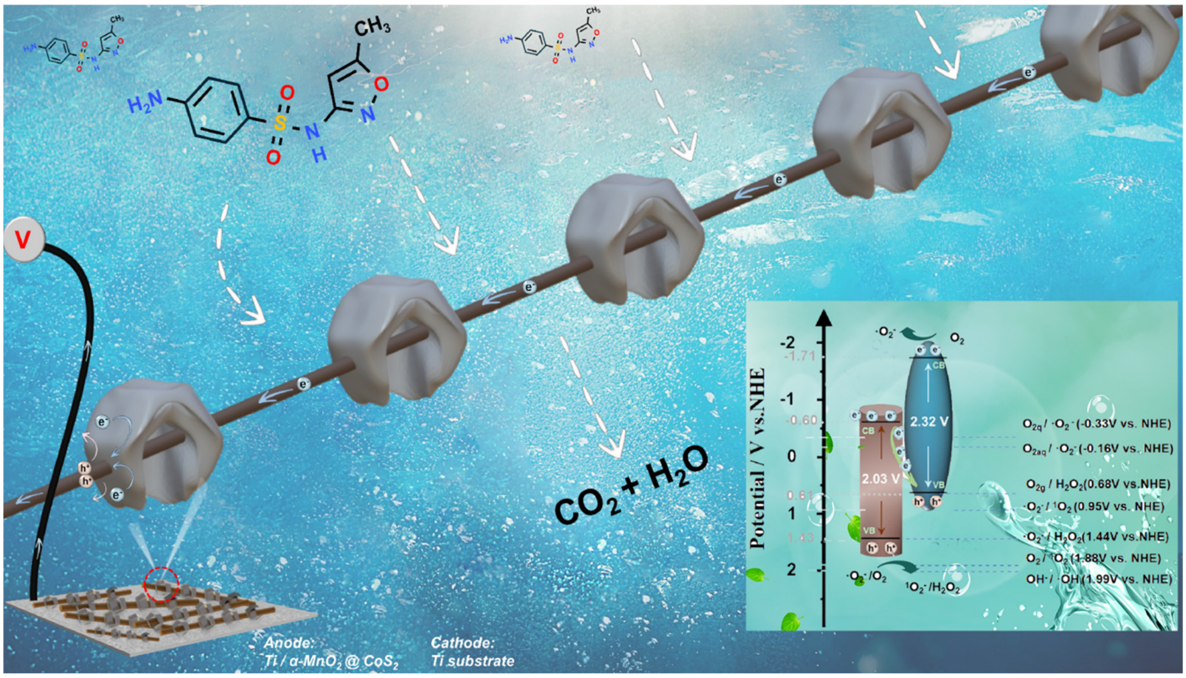

Scheme 2. Proposed mechanism for Ti/α-MnO_2@CoS_2 electrode during PEC oxidation process.

Moreover, the intermediate substance generated contained hydrogen peroxide, which was synchronous with the degradation process (Figure S8). Since the valence and conduction bands of α-MnO_2@CoS_2 span the potentials of oxidation and reduction reactions (1.23 V vs. RHE for H_2O oxidation to O_2 and 0.68 V vs. RHE for O_2 reduction), e^- and h^+ can be thermodynamically available to drive the reaction. It can be seen that the heterojunction can promote the occurrence of oxygen reduction according to the energy band location, namely the oxygen on the catalyst surface, which would generate hydrogen peroxide through a two-step process. Dissolved O_{2g} adsorbed on the catalyst surface and formed OOH* intermediates, which reacted with e^- in CB of α-MnO_2 to produce hydrogen peroxide via the 2e-ORR pathway [53]. Hydrogen peroxide would undergo Fenton-like reactions to form hydroxyl radicals (Equation (1)) [54]. This process included H_2O_2 first adsorbing on the catalytic site, O-O bond stretching and breaking to generate •OH and adsorbed -OH, the adsorbed -OH gets an electron and H^+ to generate adsorbed -H_2O, and the adsorbed -H_2O would be desorbed from the surface of the catalytic site. This Fenton-like reaction could promote the generated H_2O_2 to capture photogenerated electrons rapidly, generate •OH, facilitate the separation of photogenerated electrons and holes, and enhance the performance of degrading pollutants. In addition, photogenerated electrons can accelerate the Mn (III)/Mn (II) cycle and improve the activation of H_2O_2 [55]. The degradation of SMX with H_2O_2 included the addition and hydroxylation of aromatic rings to form nitro intermediates $C_{10}H_9N_3O_6S$. The addition of •OH on SMX structure and the removal of amino groups can further lead to the formation of $C_{10}H_{10}N_2O_4S$, in which the aromatic ring would be further hydroxylated. The obtained dihydroxylation product $C_{10}H_{10}N_2O_5S$ was decomposed by pyrolysis [56].

$$Mn^{2+} + H_2O_2 \rightarrow Mn^{3+} + \cdot OH + OH^- \qquad (1)$$

Therefore, in the degradation process of organic pollutants, the synergistic effect of $\bullet O_2^-$ and $^1O_2$ played a significant role, plus •OH and H_2O_2 assist in the oxidation of SMX and finally convert to carbon dioxide and water through mineralization.

3. Conclusions

In conclusion, using the MOF template, we designed and synthesized a unique α-MnO_2 nanowire assembled CoS_2 hollow cage by hydrothermal and vulcanization processes. The structure and composition of the prepared α-MnO_2@CoS_2 can be easily regulated by changing the amount of TAA, which XRD, SEM, and XPS disclosed. A series of electrochemical tests showed that the composite electrode has better electron transfer ability than the single electrode, which was conducive to the generation and migration of carriers. Under the condition of PEC, the SMX removal rate of α-MnO_2@CoS_2-0.2 reached 98.95% during 50 min. The high removal rate was because the constructed p-n heterojunction reduced the recombination rate of electron-hole pairs, and the unique interweaving α-MnO_2 nanowires and CoS_2 nano hollow cage structure improved the charge transfer ability and PEC degradation performance. Combined with the DFT calculation results, it was proved that α-MnO_2@CoS_2 conformed to the Z-scheme mechanism of carrier migration. The low cost, easy preparation, and excellent performance of α-MnO_2@CoS_2 photoanode made it an excellent anode material for water treatment.

Supplementary Materials: The following supporting information can be downloaded at: https://media.sciltp.com/articles/others/2506270938185377/SEE-970-SI-FC-done.pdf. Figure S1: XRD patterns of pure α-MnO_2 powder, CoS_2 powder, Ti/α-MnO_2, Ti/α-MnO_2@ZIF-67 and Ti/α-MnO_2@ CoS_2-0.2, respectively. Figure S2: XRD patterns of CoS_2 nanocages wrapped α-MnO_2 nanoflower needles with different CoS_2 concentration. Figure S3: XPS survey spectra of α-MnO_2, CoS_2 and α-MnO_2@CoS_2-0.2. Figure S4: Transient photocurrent responses of α-MnO_2, α-MnO_2@ZIF-67 and various α-MnO_2@CoS_2-x electrodes. Figure S5: (a) UV-Vis diffuse reflectance spectra of α-MnO_2, CoS_2 and α-MnO_2@CoS_2-0.2; (b) The bandgap calculation of α-MnO_2, CoS_2 and α-MnO_2@CoS_2 by the Kubelka-Munk theorem. Figure S6: Proposed band structures of α-MnO_2@CoS_2. Figure S7: SEM and XRD analysis of α-MnO_2@CoS_2-0.2 after durability test. Figure S8: Verification of hydrogen peroxide generation. Table S1: Experimental conditions of Ti/α-MnO_2@CoS_2 hierarchical heterogeneous core-shell structures. Table S2: Different catalyst applied in water purification and main result. References [57–64] are cited in the supplementary materials.

Author Contributions: H.M.: conceptualization, methodology, funding acquisition, writing-reviewing and editing; Y.C.: data curation, writing—original draft preparation, visualization; H.J.: writing—original draft preparation, investigation, data curation; X.W.: writing-reviewing and editing, investigation; G.W.: validation, supervision; Y.F.: validation; P.W.: conceptualization, validation; V.S.: supervision, investigation; K.R.: supervision, software; X.L.: writing—reviewing and editing, conceptualization, supervision. All authors have read and agreed to the published version of the manuscript.

Funding: This work was supported by the National Natural Science Foundation of China (21875026) and Liaoning BaiQianWan Talents Program, the scientific research fund of the educational department of Liaoning province (J2019013). This work was also supported by Joint Research Fund Liaoning-Shenyang National Laboratory for Materials Science (Project number: 2019JH3/30100034; Contract number: 2019010278-JH3/301), 2023 Basic Scientific Research Projects of Universities by the Educational Department of Liaoning Province (JYTZD2023027).

Institutional Review Board Statement: Not applicable.

Informed Consent Statement: Not applicable.

Data Availability Statement: Data will be made available on request.

Conflicts of Interest: The authors declare no conflict of interest.

References

1. Shang, K.; Morent, R.; Wang, N.; Wang, Y.; Peng, B.; Jiang, N.; Lu, N.; Li, J. Degradation of sulfamethoxazole (SMX) by water falling film DBD Plasma/Persulfate: Reactive species identification and their role in SMX degradation. *Chem. Eng. J.* **2022**, *431*, 133916. https://doi.org/10.1016/j.cej.2021.133916.
2. Fan, X.; Zhang, Z.; Li, X.; Liu, Y.; Cao, S.; Geng, W.; Wang, Y.; Zhang, X. Microecology of aerobic denitrification system construction driven by cyclic stress of sulfamethoxazole. *Bioresour. Technol.* **2024**, *402*, 130801. https://doi.org/10.1016/j.biortech.2024.130801.
3. Xue, Y.; Kamali, M.; Aminabhavi, T.M.; Appels, L.; Dewil, R. Tailoring the surface functional groups of biochar for enhanced adsorption and degradation of pharmaceutically active compounds. *Chem. Eng. J.* **2024**, *491*, 152037. https://doi.org/10.1016/j.cej.2024.152037
4. Wang, C.; Xing, W.; Wu, Y.; Li, Y.; Yan, Y.; Zhu, J. In-situ synthesis of CNT/UiO-66-NH_2-based molecularly imprinted

nanocomposite membranes for selective recognition and separation of sulfamethoxazole: A synergistic promotion system. *Surf. Interfaces* **2022**, *31*, 101986. https://doi.org/10.1016/j.surfin.2022.101986.

5. Xu, J.; Xu, W.; Wang, D.; Sang, G.; Yang, X. Evaluation of enhanced coagulation coupled with magnetic ion exchange (MIEX) in natural organic matter and sulfamethoxazole removals: The role of Al-based coagulant characteristic. *Sep. Purif. Technol.* **2016**, *167*, 70–78. https://doi.org/10.1016/j.seppur.2016.05.007.
6. Zhao, C.; Duan, X.; Liu, C.; Huang, H.; Wu, M.; Zhang, X.; Chen, Y. Metabolite Cross-Feeding Promoting NADH Production and Electron Transfer during Efficient SMX Biodegradation by a Denitrifier and *S. oneidensis* MR-1 in the Presence of Nitrate. *Environ. Sci. Technol.* **2023**, *57*, 18306–18316. https://doi.org/10.1021/acs.est.2c09341.
7. Zhu, E.; Yuan, D.; Wang, Z.; Zhang, Q.; Tang, S. Insight into the activation mechanism of peracetic acid by molybdenum carbide for sulfamethoxazole decomposition. *Chem. Eng. J.* **2023**, *474*, 145824. https://doi.org/10.1016/j.cej.2023.145824.
8. Peng, Y.; Xie, G.; Shao, P.; Ren, W.; Li, M.; Hu, Y.; Yang, L.; Shi, H.; Luo, X. A comparison of SMX degradation by persulfate activated with different nanocarbons: Kinetics, transformation pathways, and toxicity. *Appl. Catal. B Environ.* **2022**, *310*, 121345. https://doi.org/10.1016/j.apcatb.2022.121345.
9. Jia, Y.; Li, H.; Duan, L.; Gao, Q.; Zhang, H.; Li, S.; Li, M. Activation of persulfate by β-PDI/MIL-101(Fe) photocatalyst under visible light toward efficient degradation of sulfamethoxazole. *Chem. Eng. J.* **2024**, *481*, 148588. https://doi.org/10.1016/j.cej.2024.148588.
10. Son, A.; Lee, J.; Lee, C.; Cho, K.; Lee, J.; Hong, S.W. Persulfate enhanced photoelectrochemical oxidation of organic pollutants using self-doped TiO_2 nanotube arrays: Effect of operating parameters and water matrix. *Water Res.* **2021**, *191*, 116803. https://doi.org/10.1016/j.watres.2021.116803.
11. Li, S.; Zhang, G.; Meng, D.; Yang, F. Photoelectrocatalytic activation of sulfate for sulfamethoxazole degradation and simultaneous H_2 production by bifunctional N, P co-doped black-blue TiO_2 nanotube array electrode. *Chem. Eng. J.* **2024**, *485*, 149828. https://doi.org/10.1016/j.cej.2024.149828.
12. Qian, R.F.; Zong, H.X.; Schneider, J.; Zhou, G.D.; Zhao, T.; Li, Y.L.; Yang, J.; Bahnemann, D.W.; Pan, J.H. Charge carrier trapping, recombination and transfer during TiO_2 photocatalysis: An overview. *Catal. Today* **2019**, *335*, 78–90. https://doi.org/10.1016/j.cattod.2018.10.053.
13. Zhao, Y.; Fang, X.; Chen, L.; Zhu, J.F.; Zheng, Y.H. Improved proton adsorption and charge separation on cadmium sulfides for photocatalytic hydrogen production. *Energy Technol.* **2022**, *10*, 2200300. https://doi.org/10.1002/ente.202200300.
14. Lee, G.J.; Wu, J.J. Recent developments in ZnS photocatalysts from synthesis to photocatalytic applications—A review. *Powder Technol.* **2017**, *318*, 8–22. https://doi.org/10.1016/j.powtec.2017.05.022.
15. Muthukumar, R.; Balaji, G.; Vadivel, S. The charge transfer pathway of g-C_3N_4 decorated Au/$Ni_3(VO_4)_2$ composites for highly efficient photocatalytic hydrogen evolution. *Colloids Surf. A* **2022**, *655*, 130183. https://doi.org/10.1016/j.colsurfa.2022.130183.
16. Li, J.W.; Yang, X.Q.; Ma, C.R.; Lei, Y.; Cheng, Z.Y.; Rui, Z.B. Selectively recombining the photoinduced charges in bandgap-broken Ag_3PO_4/$GdCrO_3$ with a plasmonic Ag bridge for efficient photothermocatalytic VOCs degradation and CO_2 reduction. *Appl. Catal. B Environ*. **2021**, *291*, 120053. https://doi.org/10.1016/j.apcatb.2021.120053.
17. Chi, Z.; Zhao, J.; Zhang, Y.; Yu, H.; Yu, H. Coral-like WO_3/$BiVO_4$ photoanode constructed via morphology and facet engineering for antibiotic wastewater detoxification and hydrogen recovery. *Chem. Eng. J.* **2022**, *428*, 131817. https://doi.org/10.1016/j.cej.2021.131817.
18. Thamilselvan, A.; Dang, V.; Doong, R. Ni-Co bimetallic decorated dodecahedral ZIF as an efficient catalyst for photoelectrochemical degradation of sulfamethoxazole coupled with hydrogen production. *Sci. Total Environ.* **2023**, *873*, 162208. https://doi.org/10.1016/j.scitotenv.2023.162208.
19. Wu, S.; Hu, Y. A comprehensive review on catalysts for electrocatalytic and photoelectrocatalytic degradation of antibiotics. *Chem. Eng. J.* **2021**, *409*, 127739. https://doi.org/10.1016/j.cej.2020.127739.
20. Zheng, Z.; Zhang, Z.; Wong, K.; Lung, C.; Khan, M.; He, J.; Kumar, A.; Lo, I. Facilitating peroxymonosulfate activation for effective antibiotics degradation from drinking water by photoelectrocatalytic system using MoS_2 embedded carbon substrate. *Chem. Eng. J.* **2023**, *452*, 139591. https://doi.org/10.1016/j.cej.2022.139591.
21. Mirzaei, A.; Eddah, M.; Roualdes, S.; Ma, D.; Chaker, M. Multiple-homojunction gradient nitrogen doped TiO_2 for photocatalytic degradation of sulfamethoxazole, degradation mechanism, and toxicity assessment. *Chem. Eng. J.* **2021**, *422*, 130507. https://doi.org/10.1016/j.cej.2021.130507.
22. Balakrishnan, A.; Appunni, S.; Chinthala, M.; Vo, D.N. Biopolymer-supported TiO_2 as a sustainable photocatalyst for wastewater treatment: a review. *Environ. Chem. Lett.* **2022**, *20*, 3071–3098. https://doi.org/10.1007/s10311-022-01443-8.
23. Zhang, S.; Yi, J.; Chen, J.; Yin, Z.; Tang, T.; Wei, W.; Cao, S.; Xu, H. Spatially confined Fe_2O_3 in hierarchical SiO_2@TiO_2 hollow sphere exhibiting superior photocatalytic efficiency for degrading antibiotics. *Chem. Eng. J.* **2020**, *380*, 122583. https://doi.org/10.1016/j.cej.2019.122583.
24. Jing, Y.; Fan, A.; Guo, J.; Shen, T.; Yuan, S.; Chu, Y. Synthesis of an ultrathin MnO_2 nanosheet-coated Bi_2WO_6 nanosheet as a heterojunction photocatalyst with enhanced photocatalytic activity. *Nano-Micro Lett.* **2022**, *429*, 132193.

https://doi.org/10.1016/j.cej.2021.132193.

25. Barbosa, M.L.; Costa, M.J.S.; Lima, A.E.B.; Batista, A.M.; Longo, E.; Cavalcante, L.S.; Santos, R.S. Anionic and cationic dyes removal by degradation via photoelectrocatalysis using a $WO_3/CuWO_4$ heterojunction film as a photoanode. *Nano-Struct. Nano-Objects* **2023**, *35*, 100993. https://doi.org/10.1016/j.nanoso.2023.100993.
26. Gómez, E.; Cestaro, R.; Philippe, L.; Serrà, A. Electrodeposition of nanostructured $Bi_2MoO_6@Bi_2MoO_{6-x}$ homojunction films for the enhanced visible-light-driven photocatalytic degradation of antibiotics. *Appl. Catal. B Environ.* **2022**, *317*, 121703. https://doi.org/10.1016/j.apcatb.2022.121703.
27. Liu, Z.; Tian, J.; Yu, C.; Fan, Q.; Liu, X. Solvothermal fabrication of Bi_2MoO_6 nanocrystals with tunable oxygen vacancies and excellent photocatalytic oxidation performance in quinoline production and antibiotics degradation. *Chin. J. Catal.* **2022**, *43*, 472–484. https://doi.org/10.1016/S1872-2067(21)63876-7.
28. Wang, Z.M.; Wang, Z.H.; Li, W.; Lan, Y.Q.; Chen, C. Performance comparison and mechanism investigation of Co_3O_4-modified different crystallographic MnO_2 (α, β, γ, and δ) as an activator of peroxymonosulfate (PMS) for sulfisoxazole degradation. *Chem. Eng. J.* **2022**, *427*, 130888. https://doi.org/10.1016/j.cej.2021.130888.
29. Li, H.J.; Chen, Y.; Liu, X.H.; Sun, D.D.; Wang, P.Y.; Wang, G.W.; Zhang, X.X.; Ma, H.C. A type-II α-$MnO_2@Co_3O_4$ architecture with superior photoelectrocatalytic performance toward water purification. *Surf. Interfaces* **2023**, *39*, 102901. https://doi.org/10.1016/j.surfin.2023.102901.
30. Dang, V.; Annadurai, T.; Khedulkar, A.P.; Lin, J.; Adorna, J.; Yu, W.; Pandit, B.; Huynh, T.; Doong, R. S-scheme N-doped carbon dots anchored g-C_3N_4/Fe_2O_3 shell/core composite for photoelectrocatalytic trimethoprim degradation and water splitting. *Appl. Catal. B Environ.* **2023**, *320*, 121928. https://doi.org/10.1016/j.apcatb.2022.121928.
31. Leng, H.; Li, Z.; Li, W.; Lv, Z.; Guo, J.; You, H.; Jia, Y.; Zhang, G.; Wang, L. Synergy of dual photoelectrodes for simultaneous antibiotic degradation and CO_2 reduction by Z-scheme PEC system. *Sep. Purif. Technol.* **2024**, *338*, 126504. https://doi.org/10.1016/j.seppur.2024.126504.
32. Liu, J.; Li, J.; Li, Y.; Guo, J.; Xu, S.; Zhang, R.; Shao, M. Photoelectrochemical water splitting coupled with degradation of organic pollutants enhanced by surface and interface engineering of $BiVO_4$ photoanode. *Appl. Catal. B Environ.* **2020**, *278*, 119268. https://doi.org/10.1016/j.apcatb.2020.119268.
33. Nguyen, T.; Huang, C.P.; Doong, R.; Chen, C.; Dong, C. Visible-light photodegradation of sulfamethoxazole (SMX) over Ag-P-codoped g-C_3N_4 (Ag-P@UCN) photocatalyst in water. *Chem. Eng. J.* **2020**, *384*, 123383. https://doi.org/10.1016/j.cej.2019.123383.
34. Jia, L.; Li, F.; Yang, C.; Yang, X.; Kou, B.; Xing, Y.; Peng, J.; Ni, G.; Cao, Z.; Zhang, S.; et al. Direct Z-Scheme Heterojunction α-MnO_2/BiOI with Oxygen-Rich Vacancies Enhanced Photoelectrocatalytic Degradation of Organic Pollutants under Visible Light. *Catalysts* **2022**, *12*, 1596. https://doi.org/10.3390/catal12121596.
35. Guan, C.; Liu, X.M.; Ren, W.N.; Li, X.; Cheng, C.W.; Wang, J. Rational design of metalorganic framework derived hollow $NiCo_2O_4$ arrays for flexible supercapacitor and electrocatalysis. *Adv. Energy Mater.* **2017**, *7*, 1602391. https://doi.org/10.1002/aenm.201602391.
36. Xiao, F.; Guo, R.; He, X.; Chen, H.; Fang, W.; Li, W.; Wang, H.; Sun, Z.; Tian, P.; Zhao, L. Enhanced photocurrent by MOFs layer on Ti-doped α-Fe_2O_3 for PEC water oxidation. *Int. J. Hydrogen Energy* **2021**, *46*, 7954–7963. https://doi.org/10.1016/j.ijhydene.2020.12.023.
37. Dutta, R.; Shrivastav, R.; Srivastava, M.; Verma, A.; Saxena, S.; Biswas, N.; Satsangi, V.; Dass, S. MOFs in photoelectrochemical water splitting: New horizons and challenges. *Int. J. Hydrogen Energy* **2022**, *47*, 5192–5210. https://doi.org/10.1016/j.ijhydene.2021.11.185.
38. Toe, C.; Zhou, S.; Michael, G.; Lu, X.; Ng, Y.; Amal, R. Recent advances and the design criteria of metal sulfide photocathodes and photoanodes for photoelectrocatalysis. *J. Mater. Chem. A* **2021**, *9*, 20277–20319. https://doi.org/10.1039/D1TA05407D.
39. Li, X.C.; Wang, J.W.; Xia, J.W.; Fang, Y.X.; Hou, Y.D.; Fu, X.Z.; Shalom, M.; Wang, X.C. One-Pot Synthesis of CoS_2 Merged in Polymeric Carbon Nitride Films for Photoelectrochemical Water Splitting. *ChemSusChem* **2022**, *15*, e202200330. https://doi.org/10.1002/cssc.202200330.
40. Zhang, L.; Feng, L.; Zhuang, X.; Tang, P.; Chen, G.; Wang, H. A visible-light-driven photoelectrochemical sensor for the sensitive and selective detection of chlorpyrifos via CoS_2 quantum dots/CdS nanowires nanocomposites with 0D/1D heterostructure. *Chem. Eng. J.* **2023**, *476*, 146770. https://doi.org/10.1016/j.cej.2023.146770.
41. Lee, K.M.; Lee, Y.R.; Kim, I.Y.; Kim, T.W.; Han, S.Y.; Hwang, S.J. Heterolayered Li^+–MnO_2–$[Mn_{1/3}Co_{1/3}Ni_{1/3}]$ O_2 Nanocomposites with Improved Electrode Functionality: Effects of Heat Treatment and Layer Doping on the Electrode Performance of Reassembled Lithium Manganate. *J. Phys. Chem. C* **2012**, *116*, 3311–3319. https://doi.org/10.1021/jp210063c.
42. Wang, X.H.; Huang, F.H.; Rong, F.; He, P.; Que, R.H.; Jiang, S.P. Unique MOF-derived hierarchical MnO_2 nanotubes@NiCo-LDH/CoS_2 nanocage materials as high performance supercapacitors. *J. Mater. Chem. A* **2019**, *7*, 12018–12028. https://doi.org/10.1039/C9TA01951K.

43. Li, H.; Lyu, J.; Chen, Y.; Jian, L.; Li, R.; Liu, X.; Dong, X.; Ma, C.; Ma, H. Consecutive metal oxides with self-supported nanoarchitecture achieves highly stable and enhanced photoelectrocatalytic oxidation for water purification. *Solid State Electrochem.* **2021**, *25*, 1083–1092. https://doi.org/10.1007/s10008-020-04886-7
44. Wang, H.; Liang, Y.; Liu, L.; Hu, J.; Wu, P.; Cui, W. Enriched photoelectrocatalytic degradation and photoelectric performance of BiOI photoelectrode by coupling rGo. *Appl. Catal. B Environ.* **2017**, *208*, 22–34. https://doi.org/10.1016/j.apcatb.2017.02.055.
45. Costa, M.J.S.; Costa, G.S.; Lima, A.E.B.; Luz, G.E., Jr.; Longo, E.; Cavalcante, L.S.; Santos, R.S. Investigation of charge recombination lifetime in γ-WO_3 films modified with Ag^0 and Pt^0 nanoparticles and its influence on photocurrent density. *Ionics* **2018**, *24*, 3291–3297. https://doi.org/10.1007/s11581-018-2640-1.
46. Li, J.W.; Wang, X.Y.; Fang, H.L.; Guo, X.M.; Zhou, R.F.; Wang, C.; Li, J.; Ghazzal, M.N.; Rui, Z.B. Unraveling the role of surface and interfacial defects in hydrogen production to construct an all-in-one broken-gap photocatalyst. *J. Mater. Chem. A* **2023**, *11*, 25639–25649. https://doi.org/10.1039/D3TA03079B.
47. Guo, F.; Shi, W.L.; Wang, H.B.; Han, M.M.; Huang, H.; Liu, Y.; Kang, Z.H. Facile fabrication of a CoO/g-C_3N_4 p–n heterojunction with enhanced photocatalytic activity and stability for tetracycline degradation under visible light. *Catal. Sci. Technol.* **2017**, *7*, 3325–3331. https://doi.org/10.1039/C7CY00960G.
48. Pinaud, B.A.; Chen, Z.; Abram, D.N.; Jaramilo, T.F. Thin Films of Sodium Birnessite-Type MnO_2: Optical Properties, Electronic Band Structure, and Solar Photoelectrochemistry. *J. Phys. Chem. C* **2011**, *115*, 11830–11838. https://doi.org/10.1021/jp200015p.
49. Sboui, M.; Niu, W.K.; Li, D.Z.; Lu, G.; Zhou, N.; Zhang, K.; Pan, J.H. Fabrication of electrically conductive TiO_2/PANI/PVDF composite membranes for simultaneous photoelectrocatalysis and microfiltration of azo dye from wastewater. *Appl. Catal. A-Gen.* **2022**, *644*, 118837. https://doi.org/10.1016/j.apcata.2022.118837.
50. Li, J.W.; Fang, H.L.; Wu, M.Q.; Ma, C.R.; Lian, R.Q.; Jiang, S.P.; Ghazzal, M.N.; Rui, Z.B. Selective Cocatalyst Decoration of Narrow-Bandgap Broken-Gap Heterojunction for Directional Charge Transfer and High Photocatalytic Properties. *Small* **2023**, *19*, 2300559. https://doi.org/10.1002/small.202300559.
51. Li, J.W.; Huang, Z.Y.; Wang, C.; Tian, L.; Yang, X.Q.; Zhou, R.F.; Ghazzal, M.N.; Liu, Z.Q. Linkage effect in the bandgap-broken V_2O_5-$GdCrO_3$ heterojunction by carbon allotropes for boosting photocatalytic H_2 production. *Appl. Catal. B Environ.* **2024**, *340*, 123181. https://doi.org/10.1016/j.apcatb.2023.123181.
52. Li, J.W.; Xiang, T.C.; Liu, X.; Ghazzl, M.N.; Liu, Z.Q. Structure-function Relationship of P-Block Bismuth for Selective Photocatalytic CO_2 Reduction. *Angew. Chem. Int. Ed.* **2024**, *63*, e202407287. https://doi.org/10.1002/anie.202407287.
53. Sheng, H.; Janes, A.N.; Ross, R.D.; Ross, R.D.; Kaiman, D.; Huang, J.Z.; Song, B.; Schmidt, J.R.; Jin, S. Stable and Selective Electrosynthesis of Hydrogen Peroxide and the Electro-Fenton Process on $CoSe_2$ Polymorph Catalysts. *Energy Environ. Sci.* **2020**, *13*, 4189–4203. https://doi.org/10.1039/D0EE01925A.
54. Wu, Q.; Zou, H.; Mao, X.; He, J.H.; Shi, Y.M.; Chen, S.M.; Yan, X.C.; Wu, L.Y.; Lang, C.G.; Zhang, B.; et al. Unveiling the dynamic active site of defective carbon-based electrocatalysts for hydrogen peroxide production. *Nat. Commun.* **2023**, *14*, 6275. https://doi.org/10.1038/s41467-023-41947-7.
55. Ao, X.W.; Liu, W.J. Degradation of sulfamethoxazole by medium pressure UV and oxidants: Peroxymonosulfate, persulfate, and hydrogen peroxide. *Chem. Eng. J.* **2017**, *313*, 629–637. https://doi.org/10.1016/j.cej.2016.12.089.
56. Luo, K.; Yang, Q.; Pang, Y.; Wang, D.B.; Li, X.; Lei, M.; Huang, Q. Unveiling the mechanism of biochar-activated hydrogen peroxide on the degradation of ciprofloxacin. *Chem. Eng. J.* **2019**, *374*, 520–530. https://doi.org/10.1016/j.cej.2019.05.204.
57. Kresse, G.; Joubert, D. From ultrasoft pseudopotentials to the projector augmented-wave method. *Phys. Rev. B* **1999**, *59*, 1758–177.
58. Perdew, J. P.; Burke, K.; Ernzerhof, M. Generalized gradient approximation made simple. *Phys. Rev. Lett.* **1996**, *77*, 3865–3868.
59. Magesh, G.; Arun, A.P.; Poonguzhali, R.V.; Kumar, E.R.; Pradeep, I.; Kumar, R.R.; Abd El-Rehim, A.F. Pure α-MnO_2 and Ag decorated α-MnO_2 nanorods for photocatalytic activity. *J. Mol. Struct.* **2025**, *1329*, 141444. https://doi.org/10.1016/j.molstruc.2025.141444.
60. Ma, H.; Li, H.; Wang, J.; Wang, X.; Wang, G.; Liu, X. Developing Z-scheme Bi_2MoO_6@ α-MnO_2 beaded core-shell heterostructure in photoelectrocatalytic treatment of organic wastewater. *J. Environ. Manag.* **2024**, *3677*, 121964. https://doi.org/10.1016/j.jenvman.2024.121964.
61. Wu, Y.; Fang, X.; Shen, X.; Yu, X.; Xia, C.; Xu, L.; Zhang, Y.; Gan, L. Synergetic effect of photocatalytic oxidation plus catalytic oxidation on the performance of coconut shell fiber biochar decorated α-MnO_2 under visible light towards BPA degradation. *J. Environ. Manag.* **2023**, *345*, 118911. https://doi.org/10.1016/j.jenvman.2023.118911.
62. Ullah, A.; Rahman, L.; Hussain, S.Z.; Abbas, W.; Tawab, A.; Jilani, A.; Bajwa, S.Z.; Khan, W.S.; Riaz, R.; Hussain, I.; et al. Mechanistic insight of dye degradation using TiO_2 anchored α-MnO_2 nanorods as promising sunlight driven photocatalyst. *Mater. Sci. Eng. B* **2021**, *271*, 115257. https://doi.org/10.1016/j.mseb.2021.115257.
63. Yusuf, T.L.; Ogundare, S.A.; Opoku, F.; Mabuba, N. Photoelectrocatalytic degradation of sulfamethoxazole over S–

Scheme $Co_3Se_4/BiVO_4$ heterojunction photoanode: An experimental and density functional theory investigations. *Surf. Interfaces* **2023**, *36*, 102534. https://doi.org/10.1016/j.surfin.2022.102534.

64. Mafa, P.J.; Kuvarega, A.T.; Mamba, B.B.; Ntsendwana, B. Photoelectrocatalytic degradation of sulfamethoxazole on g-C_3N_4/BiOI/EG pn heterojunction photoanode under visible light irradiation. *Appl. Surf. Sci.* **2019**, *483*, 506–520. https://doi.org/10.1016/j.apsusc.2019.03.281.